BULLETIN OF THE POLISH ACADEMY OF SCIENCES
TECHNICAL SCIENCES, Vol. 74(5), 2026, Article number: 1957
DOI: 10.24425/bpasts.2026.1957

Accident-driven human-like trajectory planning for permissive left turns

Wanqiu WANG* and **Haonan ZHANG**

School of Mechanical and Automotive Engineering, Shanghai University of Engineering Science, Shanghai, China

Abstract. Making a left turn at a signalized intersection without a protected green arrow presents a critical challenge for autonomous vehicles, often resulting in either overly aggressive or conservative behaviors. To resolve this conflict between safety and efficiency, this paper proposes a closed-loop adaptive trajectory planning framework incorporating Risk Homeostasis Theory. Utilizing real-world collision data from the National Automobile Accident In-Depth Investigation System (NAIS) database, we analyze failure mechanisms of rigid strategies and introduce a perception model fusing a high-order Gaussian Driving Risk Field with a Random Finite Set dynamic occupancy grid. Unlike static methods, a bio-inspired mechanism enables the vehicle to dynamically adjust its speed and safety buffers within a Frenet frame using a proportional-integral-derivative (PID) controller to maintain a target risk level. Simulations based on reconstructed accidents demonstrate that the proposed method effectively balances physical safety with ride experience. The system triggers early braking in high-threat scenarios while suppressing unnecessary hesitation in low-risk situations, successfully replicating human-like driving styles.

Keywords: autonomous driving; trajectory planning; risk homeostasis theory; permissive left turn.

1. INTRODUCTION

Permissive-phase left turns are widely adopted because they can effectively exploit available green-time gaps and improve intersection throughput [1]. However, during an unprotected left-turn phase, ambiguity in right-of-way between left-turning vehicles and oncoming through traffic can readily lead to safety issues [2]. This scenario has therefore become a high-incidence setting for lateral collisions and severe injuries at urban intersections [3,4]. Left-turn drivers often must decide whether to yield or proceed to prevent conflicts from escalating into crashes. Consequently, achieving accurate risk assessment and robust local trajectory planning in complex, dynamic environments is critical for autonomous vehicles to safely execute permissive-phase left turns.

To ensure safety in complex intersection scenarios, existing risk assessment methods can generally be grouped into three categories: deterministic-metric-based approaches, probabilistic-grid-based approaches, and potential-field-based approaches.

Early studies typically used time-domain indicators (e.g., TTC and PET) or spatial indicators to quantify conflict risk. Abdel-Aty *et al*. analyzed the relationship between signal phasing and crash patterns based on traditional traffic-flow theory [5, 6]. However, Westhofen *et al*. noted that such metrics depend heavily on accurate future-trajectory prediction [7]. In highly interactive scenarios with occlusions or behavioral uncertainty, Lefèvre *et al*. reported that prediction uncertainty can cause these indicators to fluctuate substantially and fail to capture the continuous spatiotemporal distribution of risk [8].

To address perceptual uncertainty, probabilistic occupancy grid maps (OGM) have been widely adopted. Buehler *et al*. demonstrated the effectiveness of grid maps for modeling complex environments in the DARPA Urban Challenge [9]. Nuss *et al*. further proposed a Random Finite Set (RFS)-based Dynamic Occupancy Grid Map (DOGM) to estimate both occupancy probabilities and velocities in real time [10]. Nevertheless, Jang *et al*. pointed out that standard DOGM mainly provides geometric occupancy information and lacks a semantic description of "potential threat regions," making it difficult for the planning module to distinguish risk levels [11].

In recent years, the Driving Risk Field (DRF) has been introduced to describe continuous risk in traffic environments. Wang *et al*. proposed a unified driving safety field model based on closed-loop "driver–vehicle–road" interactions [12]. Mullakkal-Babu *et al*. and Wang *et al*. extended this idea into probabilistic frameworks, using field potential energy to quantify uncertainty-related risk in vehicle motion [13,14]. Although risk-field theory enables a continuous representation of risk, most existing studies emphasize offline analysis and lack an online mechanism that deeply integrates the "uncertainty-handling capability" of dynamic grids with the "semantic quantification capability" of risk fields.

In complex dynamic scenarios such as permissive left turns, a trajectory planner must generate safe and smooth trajectories in real time under multiple constraints. Existing planning methods can be broadly categorized into sampling-based, optimization-based, and deep-learning-based approaches. Sampling-based approaches are widely used due to their simple structure and computational efficiency. A classic paradigm is the quintic-polynomial sampling method proposed by Werling *et al*., which can generate smooth trajectories that satisfy vehicle kinematic

*e-mail: tutu_net@163.com

Manuscript submitted 2026-01-22, revised 2026-06-03, initially accepted for publication 2026-07-01, published in September 2026.

constraints [15]. Combined with high-definition maps and finite-state machines, such methods have been successfully applied to highway lane changes and simple intersection cruising [16]. However, sampling-based planners depend strongly on cost-function parameterization. Static, fixed weights often fail to adapt to time-varying risk at intersections, leading to “sluggish” over-yielding in low-risk situations and “reckless” behavior when risk rises abruptly without sufficient safety margin.

Optimization-based approaches formulate planning as a constrained optimization problem to obtain a globally optimal solution while satisfying vehicle dynamics and collision-avoidance constraints. By solving quadratic programs (QP) or nonlinear programs (NLP) in a receding horizon, Model Predictive Control (MPC) can accurately manage nonholonomic constraints and multi-objective coupling [17]. Ziegler *et al.* demonstrated autonomous driving in complex urban environments using continuous optimization in the Bertha project [18]. However, optimization methods often face rapidly increasing computational complexity in highly dynamic scenarios, and their safety constraints are typically hard, lacking the flexibility to adjust boundaries according to risk level.

With the development of AI, end-to-end planning based on deep learning and reinforcement learning has become a research hotspot [19]. These methods learn a direct mapping from perception inputs to control outputs. Deep inverse reinforcement learning (DIRL) can imitate expert human driving strategies and has shown potential for complex intersection games where interaction intent is ambiguous [20, 21]. Nevertheless, learning-based methods are often “black-box” and lack interpretability, making them difficult to reliably verify in safety-critical autonomous driving systems and prone to limited generalization under unseen extreme-risk conditions.

Given the shared limitations of existing planners – namely static parameterization and open-loop risk handling, which make it difficult to actively balance safety and efficiency – this study introduces Risk Homeostasis Theory (RHT) [22]. The goal is to transfer the human closed-loop mechanism of “adjusting behavior based on perceived risk error” into the autonomous driving control loop, thereby mitigating polarized behaviors such as excessive conservatism or delayed reactions in permissive left turns. Building on real crash cases, we propose an integrated method that fuses dynamic risk assessment with adaptive trajectory planning: (i) tightly integrating RFS-based dynamic occupancy probabilities with a high-order Gaussian driving risk field on a unified spatiotemporal cost map; (ii) constructing an RHT-based feedback mechanism that adaptively revises speed-limit and safety-buffer constraints according to real-time risk error; (iii) generating decoupled longitudinal and lateral polynomial trajectories in a Frenet frame; and (iv) validating the method under typical reconstructed conflict conditions, demonstrating both extreme collision-avoidance capability under crash-like scenarios and adaptive decision-making across different driving styles (Comfort/Standard).

2. CRASH RECONSTRUCTION AND CAUSATION ANALYSIS

To better understand the crash mechanisms of permissive phase left turns and to clarify the functional requirements for autonomous driving in highly interactive environments, this study uses the National Automobile Accident In-Depth Investigation System (NAIS) database [23] to select and reconstruct two representative crashes that occurred at signalized intersections in Songjiang District, Shanghai. These two cases correspond to typical failures at the extremes, aggressive gap forcing and overly conservative hesitation – and provide empirical evidence for developing the subsequent risk assessment model and planning strategy. The reconstructed crash sequences are shown in Fig. 1.

2.1. Crash reconstruction and causation analysis

Using PC-CRASH vehicle dynamics simulation [24], we extracted key kinematic parameters during the 3–5 s before the impact (Table 1) and analyzed the crash causes.

Case 1: Side collision caused by aggressive gap forcing during a left turn.

This crash occurred at a major/minor arterial intersection in Songjiang District, Shanghai. The ego vehicle adopted an “efficiency-first” aggressive left-turn strategy. Table 1 shows that although the driver applied extreme evasive maneuvers before impact and executed a large steering change of 120.10°, the vehicle still collided laterally with the obstacle vehicle at

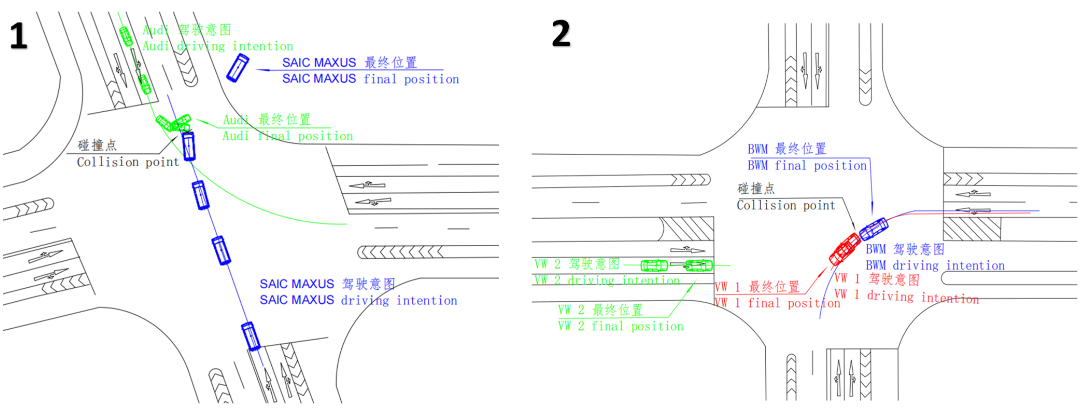

Fig. 1. Typical crash sequences reconstructed from NAIS data

Table 1
Key kinematic parameters before the impact

Scene type	Vehicle	v_{int} (km/h)	v_{impact} (km/h)	$a_{\min}$ (m/s^2)	$\Delta\theta$yaw (°)
Case 1: Side collision	Ego (AUDI)	23.05	12.20	−5.62	120.10
	Obs (MAXUS)	64.63	33.12	−5.05	69.80
Case 2: Rear-end	Ego (VW 1)	16.72	8.15	−1.67	35.80
	Follow (BMW)	35.17	15.89	−7.85	144.50
	Obs (VW 2)	21.90	10.38	−1.10	0.20

12.20 km/h. The obstacle vehicle also braked hard; however, due to its high initial speed (64.63 km/h), its speed at the moment of collision remained as high as 33.12 km/h.

This case highlights a key mismatch between geometric "free space" and physical "risk occupancy." From the perspective of a conventional occupancy grid, the oncoming vehicle had not yet entered the conflict zone, so the conflict region could appear as a binary "θ", which can mislead the planner into believing there is a viable gap. The crash suggests that geometric occupancy or discrete time-to-collision metrics alone are insufficient in high-speed dynamic scenes. A continuous potential-field view is needed – one that couples relative velocity and spatial distance – so the vehicle can "see" areas that look geometrically empty but are, in fact, high-risk due to kinetic threat.

Case 2: Rear-end crash induced by overly conservative hesitation during a left turn.

This crash occurred at a similarly channelized signalized intersection. During the left turn, the ego vehicle hesitated excessively due to an oncoming vehicle. The data show an initial speed of only 16.72 km/h, followed by continuous deceleration to 8.15 km/h, with a mild deceleration of −1.67. The following vehicle failed to anticipate the ego's conservative intent and eventually applied emergency braking of −7.85, but still rear-ended the ego at 15.89 km/h.

This case underscores the interaction-driven nature of planning and the challenge of maintaining behavioral stability. If an autonomous vehicle behaves overly conservatively in low-risk situations, it not only reduces efficiency but can also violate traffic-flow expectations and trigger secondary crashes. In this sense, an ideal trajectory planner should not rely on fixed parameters. It should instead incorporate risk homeostasis – adjusting its level of assertiveness or conservatism according to perceived risk, maintaining reasonable efficiency while avoiding abrupt behavioral shifts that destabilize interactions.

2.2. Scenario reconstruction

Following the typical channelized layout of arterials in Songjiang District, each approach is configured as a two-way four-lane roadway. Specifically, each direction provides two motor-vehicle lanes, both shared for turning and through movements, with a uniform lane width of 3.5 m. Motor-vehicle lanes and nonmotorized lanes are arranged one-way per direction and separated by lane markings. The road centerlines are approximately orthogonal at the geometric center of the intersection, and the conflict area is approximated as a rectangle.

This work focuses on the conflict mechanism and collision-avoidance strategy between a left-turning vehicle and an oncoming through vehicle under permissive conditions. To simplify signal control modeling, the scenario is treated as a sufficiently long permissive phase. The analysis concentrates on how the left-turning vehicle evaluates risk and makes avoidance decisions based on the state of the oncoming traffic stream under sustained "potentially passable" conditions.

If there is no other potential conflict inside the intersection, drivers typically traverse along their expected path. To emulate this ideal left-turn behavior without conflict interference, we construct a global reference trajectory following Lu *et al*. [25]. The reference trajectory consists of geometric path planning and desired speed planning, as illustrated in Fig. 2.

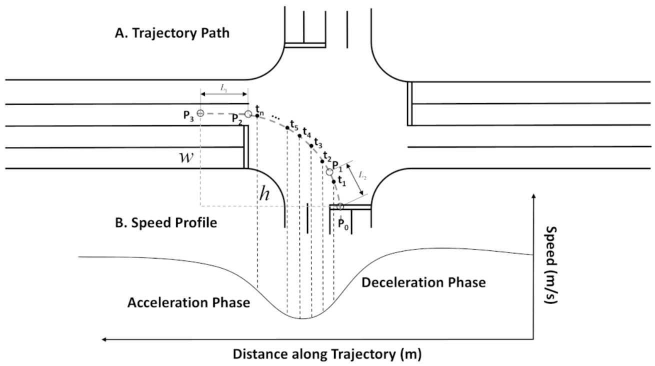

Fig. 2. Schematic of global reference trajectory planning

For the geometric path, we use a cubic Bézier curve. By extracting key intersection geometry parameters (e.g., lateral spacing between entry/exit lanes and the longitudinal offset), four control points are determined. The start and end points lie on the entry stop line and the exit-lane centerline, respectively, while the two intermediate control points (i.e., control lengths) are determined via a statistical regression model. This yields a smooth turning path with continuous curvature. For speed planning, we mimic driver dynamics under free-flow conditions and assume a "decelerate first, then accelerate" strategy when traversing the intersection.

3. DYNAMIC RISK ASSESSMENT

This section addresses permissive-phase left-turn decision-making for intelligent vehicles by proposing a dynamic risk assessment method that fuses a dynamic occupancy grid with a driving risk field. The key idea is to construct a multi-sensor, evidence-based grid representation to unify the spatial distribution and motion states of traffic participants in the intersection and then introduce a risk-field model that accounts for both static and dynamic obstacles. The two are fused on a multi-layer, predictive cost map to support downstream planning under uncertainty.

3.1. Perception layer

To ensure sufficient coverage of the intersection area, we build a perception system based on a multi-LiDAR array. The simulation advances with a 0.1 s time step, and six multi-line LiDARs (each with a 100 m range) are deployed around the ego vehicle. Multi-sensor point clouds are time-synchronized and extrinsically calibrated, transformed into the ego frame, and then processed with basic measurement filtering and ground removal to form a fused observation set. In permissive left-turn scenarios, this observation set covers the ego lane, the oncoming through lane, and the conflict zone inside the intersection, providing reliable inputs for dynamic occupancy grid modeling.

It should be noted that in this study, the multi-LiDAR array serves strictly as a simulation-oriented sensing abstraction to provide dense spatial evidence for the subsequent grid modeling. The proposed downstream planning framework, however, is intrinsically sensor-agnostic and can seamlessly operate on inputs derived from standard mass-production perception stacks, such as camera-radar fusion.

3.2. Dynamic Occupancy Grid Model

A Dynamic Occupancy Grid Model (DOGM) is a grid-based environment representation widely used in autonomous driving and robotics to encode and track surrounding spatial information. Given that permissive-phase left turns involve multiple participants, complex target shapes, and frequent appearance/disappearance, we move beyond a conventional Kalman-filter framework and adopt an RFS (Random Finite Set)-based DOGM to model the intersection environment. Using a particle filter, a large particle set approximates the posterior distribution and updates the occupancy state of each grid cell (Occupied/Free/Unknown) and velocity vector in real time (Key parameters are detailed in Table 2).

Table 2
Key parameters of the dynamic occupancy grid model

Category	Parameter	Value
Local map configuration	Map size	120 m × 120 m
	Coordinate system	Ego frame
	Grid resolution	2 m
Particle model parameters	Total number of particles	1×10^5
	Number of birth particles	2×10^4
	Birth probability	0.025
Motion prior parameters	Velocity prior range	[−15, 15] m/s

3.3. Driving Risk Field model

While the dynamic occupancy grid indicates whether a region may be occupied, it does not directly quantify how dangerous a location is. To capture the continuous distribution of threat, we construct a Driving Risk Field (DRF) over the local intersection area. Each traffic participant is modeled as a "risk source," producing a spatial field with a certain shape and intensity; higher intensity implies greater danger for the ego vehicle under the current relative-motion relationship. The DRF consists of a static risk field and a dynamic risk field: the static component is determined by obstacle geometry, whereas the dynamic component mainly reflects interactive motion between moving obstacles and the ego vehicle. The overall risk field of an obstacle is obtained by superimposing the static and dynamic fields, as in (1)

$$U_{\text{obs}} = U_{\text{sta}} + U_{\text{dyn}}\,. \tag{1}$$

(1) Static risk field: The static field characterizes risk induced by static obstacles by considering relative distance and approach direction. Unlike the commonly used 2D Gaussian, we use a high-order Gaussian so that obstacle boundaries also exhibit non-negligible field intensity, as illustrated in Fig. 3. The formulation is given in (2) and (3), where the static risk at a location depends on the obstacle world-frame position, an obstacle-shape function, longitudinal/lateral extents, and positive constants.

$$U_{\text{sta}} = A \times \exp\left(-\frac{1}{2}\times\left(\left(\frac{(x-x_{\text{obs}})^2}{\sigma_{xg}^2}\right)^2 + \left(\frac{(y-y_{\text{obs}})^2}{\sigma_{yg}^2}\right)^2\right)^2\right), \tag{2}$$

$$\begin{cases}\sigma_{xg} = k_x W_{\text{obs}}\,,\\ \sigma_{yg} = k_y L_{\text{obs}}\,,\end{cases} \tag{3}$$

where U_{sta} denotes the static risk value at position (x, y) and $(x_{\text{obs}}, y_{\text{obs}})$ represents the coordinates of the obstacle in the global coordinate system; σ refers to the obstacle shape function parameters; L_{obs} and W_{obs} denote the longitudinal length and lateral width of the obstacle, respectively; and A and k are positive constants.

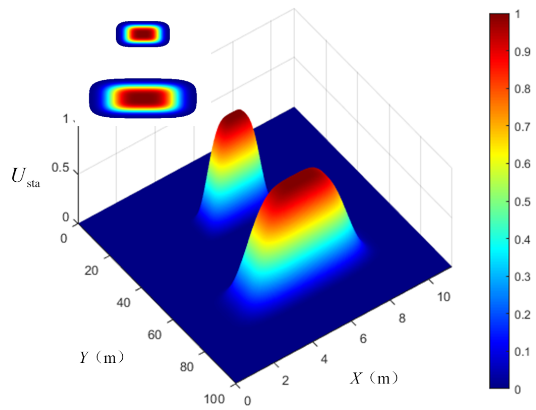

Fig. 3. Static risk-field intensity distribution

(2) Dynamic risk field: The dynamic field captures risk contributed by moving obstacles that may collide with the ego vehicle. It depends on relative motion: when the approach direction aligns with the relative-velocity direction, a smaller relative distance implies a higher collision likelihood and thus higher risk; conversely, if the obstacle is faster than the ego vehicle and is moving away, collision risk decreases. To model this pattern

across moving agents, we use a 2D Gaussian dynamic field as in (4), shown in Fig. 4.

$$U_{\text{dyn}} = A \times \frac{\exp\left(\dfrac{(y-y_{\text{obs}})^2}{\sigma_v^2} + \dfrac{(y-y_{\text{obs}})^2}{\sigma_{yg}^2}\right)}{1+\exp\left(rel_v\left(x-x_{\text{obs}}-\alpha L_{\text{obs}} rel_v\right)\right)}, \tag{4}$$

where v_{obs} and v denote the longitudinal velocities of the obstacle and the ego vehicle, respectively; rel_v represents the direction of relative motion, defined as $rel_v = 1$ if $v_{\text{obs}} > v$, and $rel_v = -1$ otherwise; and k_v and α are constants, with the constraint $0 \le \alpha \le 1$.

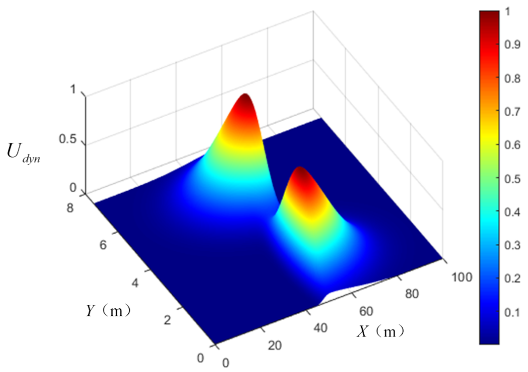

Fig. 4. Dynamic risk-field intensity distribution

Because the ego vehicle is executing a left turn, lateral motion of the obstacle can be neglected in our setting. Risk maps generated under different obstacle speeds are shown in Fig. 5, where relative speed largely determines the intensity distribution of the dynamic risk field.

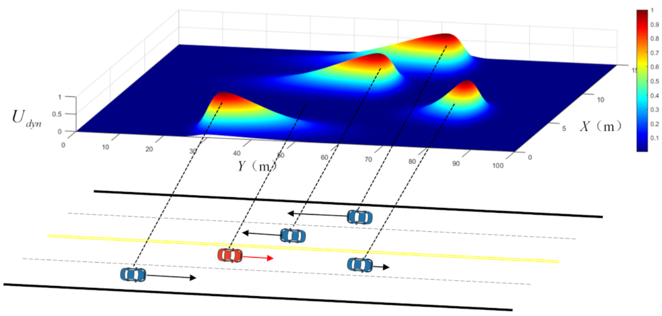

Fig. 5. DRF intensity distribution in complex traffic with relative motion to the ego vehicle

To transform the risk assessment into a quantifiable decision metric for the planning layer, this paper introduces the Real-time Comprehensive Risk Score, denoted as $R(t)$. This metric characterizes the instantaneous risk level of the ego vehicle within the risk field, serving as a pivotal interface between perception and behavioral decision-making. Given the center position of the ego vehicle (x_t, y_t) at time t, $R(t)$ is defined as the normalized value of the driving risk field potential at that location

$$R(t) = N\left(U_{\text{obs}}(x_t, y_t)\right), \tag{5}$$

where $N(\cdot)$ represents the normalization function, which maps the field intensity to the interval $[0, 1]$. As R approaches 0, the risk level decreases; conversely, a higher value indicates a higher level of risk.

3.4. Fusion of dynamic grid and driving risk field

To provide a unified and comprehensive risk metric that supports trajectory decision-making within uncertain environments, this study proposes a deep integration of the RFS-based dynamic occupancy grid output with the driving risk field model. The objective is to construct a multi-layered fused cost map covering the future prediction horizon, capable of simultaneously capturing environmental physical occupancy uncertainty and potential dynamic interaction risks. In each planning cycle, the perception system outputs multi-frame dynamic occupancy grid predictions for the future T_{horizon} seconds, discretized by a time step of $\Delta t_{\text{predict}}$. Based on these predicted data, two fundamental cost maps are generated: Occupancy Cost Map (C_{occ}): For each predicted timestamp t, an occupancy cost $C_{\text{occ}}(x,y,t)$ reflecting physical proximity is generated based on the grid cell occupancy probability $P_{\text{occ}}(x,y,t)$ using a Distance Transform and mapping functions. Cost values approach 1 in regions close to high-probability occupancy and decay rapidly to 0 with increasing distance. This cost map is primarily utilized for avoiding explicit physical obstacles. Risk Field Cost Map (C_{risk}): Similarly, for each predicted timestamp t, the driving risk field $U_{\text{obs}}(x,y,t)$ is projected onto the same spatiotemporal grid to form the risk cost $C_{\text{risk}}(x,y,t)$. This cost map emphasizes the quantification of potential dynamic conflicts and psychological pressure. To ensure the system maintains sufficient sensitivity to potential hazards, the final fused spatiotemporal cost map (C_{map}) is derived by superimposing the occupancy cost and the risk cost. For an arbitrary grid cell (x,y) at time t, its fused cost is calculated as

$$C_{\text{map}}(x,y,t) = \max\left(C_{\text{occ}}(x,y,t)\alpha,\ C_{\text{risk}}(x,y,t)\right), \tag{6}$$

where α serves as a weighting coefficient for the risk cost, designed to balance the influence of physical occupancy information and virtual risk field potential on the final cost.

This fusion mechanism effectively mitigates the limitations of relying solely on occupancy grids when dealing with noise measurement and highly dynamic targets. Even if a region is geometrically identified as "free" temporarily, the fused cost remains dominated by C_{risk} if the area is covered by high-risk field potential, thereby ensuring the planner's ability to recognize latent threats. This approach transcends traditional binary occupancy descriptions. By emulating the defensive reasoning of human drivers, it elevates environmental representation from a binary distinction of "obstacle presence" to a continuous semantic level of "risk severity." The resulting spatiotemporal multi-layered cost map, C_{map}, not only accurately delineates dynamic risk gradients arising from high-speed motion but also provides a unified, continuous, and quantifiable input interface for downstream trajectory planning, significantly enhancing the system's predictive collision avoidance capabilities.

4. RISK HOMEOSTASIS-BASED ADAPTIVE TRAJECTORY PLANNING

Building on the "dynamic occupancy grid–driving risk field" risk assessment framework developed in Section 3, this section proposes an adaptive trajectory planning method for permissive-phase left turns based on Risk Homeostasis Theory (RHT). Instead of using fixed planning parameters, the method adjusts the sampling space and behavioral parameters online according to the real-time risk level, closing the loop of perception–evaluation–planning.

4.1. Risk-guided trajectory generation

To ensure computational efficiency while sufficiently covering the potential safe solution space, this study adopts a local planning framework based on the Frenet coordinate system. The vehicle state is decoupled into longitudinal motion, s, along the global reference trajectory, and lateral offset, d, perpendicular to it. A quintic polynomial is employed to connect the current state with the terminal sampling state, ensuring continuity across position, velocity, and acceleration dimensions. Unlike traditional methods that perform blind sampling across the entire state space, this paper introduces a state sampling strategy based on risk classification. Guided by the real-time comprehensive risk score, R, derived in Section 3, the planner adaptively switches between three distinct modes. The trajectory generation strategies corresponding to different risk levels are illustrated in Fig. 6.

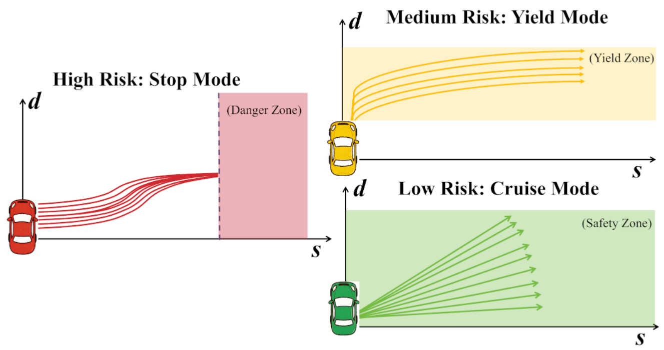

Fig. 6. Schematic of risk-guided trajectory generation in the Frenet coordinate frame

"Stop Mode" under high-risk conditions: When the real-time risk score R exceeds the passing threshold, R_{pass}, the planner constrains the terminal longitudinal position to a point preceding the conflict zone entrance and sets both the terminal velocity and acceleration to zero. In this state, the sampling space is explored exclusively along the time dimension, T, to generate a smooth stopping trajectory.

"Yield Mode" under medium-risk conditions: When the risk falls within the deceleration range ($R_{\text{slow}} < R \le R_{\text{pass}}$), it indicates the presence of potential conflicts despite the existence of a passable gap. Consequently, the planner restricts the sampling interval of the terminal target velocity, $\dot{s}(t)$, to a low-speed range $[0.5v_{\text{lim}}, 0.8v_{\text{lim}}]$ and performs fine-grained sampling laterally around the reference path. This mode aims to generate "defensive deceleration" trajectories, thereby reserving a safety margin for subsequent decision-making.

"Cruise Mode" under low-risk conditions: When $R \le R_{\text{slow}}$, the planner performs comprehensive sampling of the target velocity within permissible road speed limits $[v_{\min}, v_{\text{lim}}]$. Furthermore, it permits larger lateral offsets, d_T, to optimize trajectory curvature, thereby prioritizing traffic efficiency.

4.2. Comprehensive cost function

Generated candidate trajectories are first subjected to a feasibility screening based on vehicle kinematic limits and hard thresholds within the dynamic occupancy grid. For the feasible trajectories that survive this filtering process, a multi-dimensional cost function, J_{total}, is constructed as follows:

$$J_{\text{total}} = w_{\text{smooth}} J_{\text{smooth}} + w_{\text{eff}} J_{\text{eff}} + w_{\text{safety}} J_{\text{safety}}, \tag{7}$$

where J_{eff} (Efficiency Cost) denotes the cost associated with traffic efficiency, designed to encourage the vehicle to traverse the intersection expeditiously; and J_{smooth} (Smoothness and Consistency Cost) represents the penalty for trajectory roughness and control inconsistency. The dual-safety cost, J_{safety}, a focal point of this design, unifies physical collision avoidance with field-based risk assessment, strictly aligning with the dynamic risk identification model presented in Section 3. The terms denoted by w represent the corresponding weighting coefficients.

$$J_{\text{safety}} = k_{\text{coll}} \cdot P_{\text{occ}}^{\max} + k_{\text{risk}} \int_0^T U_{\text{total}}\left(x(t), y(t)\right) \mathrm{d}t, \tag{8}$$

where k_{coll} serves as the penalty coefficient for the collision probability term, calibrating the intensity of the system avoidance regarding physical space occupancy; and $P_{\text{occ}}^{\max}$ represents the maximum occupancy probability along the trajectory within the dynamic occupancy grid, used to identify explicit physical collision risks. The integral term corresponds to the total potential of the driving risk field, U_{total}, constructed in Section 3. By integrating the field intensity along the spatiotemporal path of the trajectory, this term quantifies the degree of exposure of the vehicle to "latent risk" zones, thereby guiding the planner to proactively navigate away from regions of high-risk potential.

4.3. Risk homeostasis adaptation

To break the fixed-parameter stalemate between "overly conservative" and "overly aggressive" behaviors and to enable the vehicle to adapt to both environmental risk and passenger expectations, we introduce Risk Homeostasis Theory (RHT) and build a closed-loop feedback mechanism. RHT argues that drivers do not seek "zero risk"; instead, they regulate their behavior to keep perceived risk around a desired target level of risk. Tan *et al*. [26] and Hua *et al*. [27] have applied RHT to car-following and intersection-approach behavior modeling and calibrated the expected risk level to 0.345, supporting the feasibility of driving an RHT loop using continuous risk indicators. Accordingly, we construct a planning-layer feedback loop under the "perception–evaluation–planning" architecture.

4.3.1. Risk homeostasis feedback model

We utilize the total potential energy of the driving risk field (established in Section 3) as the quantitative baseline for perceived risk. The perceived risk error at time t, denoted as $e_r(t)$, is defined as the difference between the target risk and the real-time perceived risk, as shown in equation (9)

$$e_r(t) = R_{\text{target}} - R(t), \tag{9}$$

where R_{target} (Target Risk Threshold) is a preset tolerance level representing the psychological safety boundary associated with different driving styles.

$$v_{\text{lim}}(t+1) = v_{\text{lim}}(t) + K_{pv} \cdot e_r(t) + K_{iv} \int e_r(\tau)\,\mathrm{d}\tau, \tag{10}$$

$$D_{\text{buf}}(t+1) = D_{\text{buf}}(t) + K_{pd} \cdot e_r(t) - K_{id} \int e_r(\tau)\,\mathrm{d}\tau. \tag{11}$$

To emulate both a driver's immediate reaction to transient risk and longer-term adaptation to sustained risk, we employ a PI (Proportional-Integral) controller. Based on the risk error, the controller adjusts two key planning constraints online – the adaptive speed limit (v_{lim}) and the safety buffer distance (D_{buf}) – as formulated in equations (10) and (11). The control mechanism and its impact on the planning constraints are schematically illustrated in Fig. 7.

When the perceived field intensity is below the psychological threshold, the controller outputs a positive gain: the speed limit is gradually increased, and the virtual buffer is reduced, allowing the planner to explore more efficient trajectories. Conversely, when the perceived field intensity exceeds the threshold, the error becomes negative; the controller quickly lowers the speed limit and enlarges the safety buffer. This forces the trajectory generation module (Section 4.1) to contract the sampling space toward the low-speed regime, while collision checking (Section 4.2) reserves a larger safety margin, resulting in a more defensive driving behavior.

4.3.2. Driving styles

To provide a methodological justification for the parameter tuning, the weights of the comprehensive cost function and the PI controller gains are derived through data-driven geometric and physical kinematic modeling, utilizing the empirical boundaries extracted from the NAIS crash reconstructions. Specifically, the tuning process strictly focuses on trajectory shape modeling. By iteratively calibrating these specific numerical values (which are detailed in Table 3 of Section 5.2 for simulation validation), we ensure that the geometric transformation of the vehicle path in the Frenet frame strictly adheres to the dynamic safety buffer (Dbuf) dictated by the real-time risk field. Utilizing the aforementioned homeostasis model and these calibrated parameters, two typical human-like driving styles can be realized by configuring distinct target risk thresholds (Rtarget)and cost weights (defined in Section 4.2):

Comfort Style: A lower target risk threshold and a larger smoothness weight (w_{smooth}) are applied. The system exhibits higher sensitivity to risk field intensity; deceleration logic is triggered immediately upon any rise in risk. The resulting trajectories tend to brake early, accelerate gently, and reduce lane-changing frequency, thereby prioritizing ride comfort and subjective safety.

Standard Style: A higher target risk threshold and a larger efficiency weight (w_{eff}) are applied. The system maintains higher speeds within a controllable risk range and behaves more decisively when feasible gaps are present. This style is particularly suitable for peak traffic hours or scenarios where throughput is emphasized.

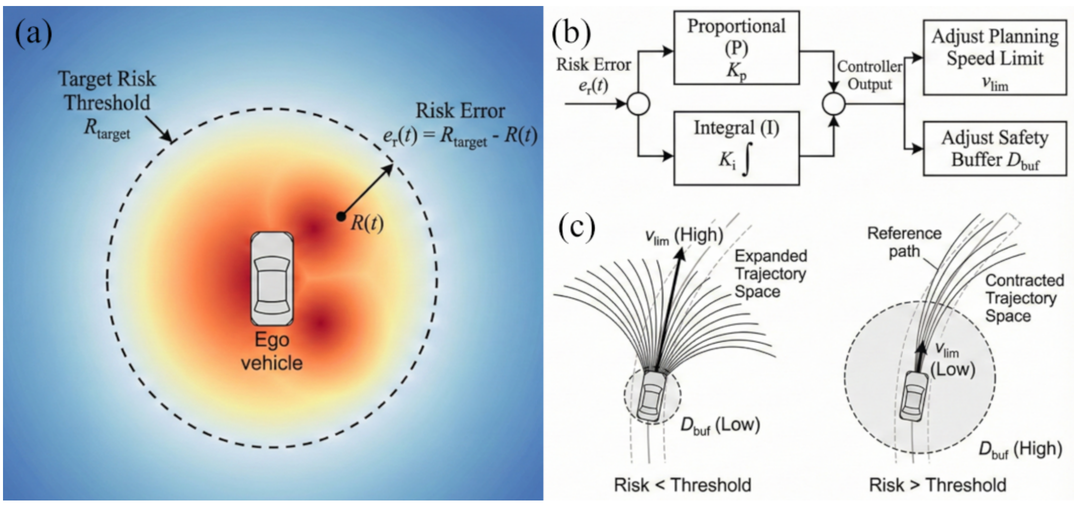

Fig. 7. Schematic of the Risk Homeostasis-based feedback mechanism. (a) Risk field intensity distribution and definition of risk error; (b) Structure of the PI controller for parameter adaptation; (c) Illustration of adaptive trajectory planning constraints (speed limit v_{lim} and safety buffer D_{buf}) under different risk levels

5. SIMULATION EXPERIMENT ANALYSIS

To validate the effectiveness of the proposed collision-avoidance strategy in permissive-phase left-turn scenarios, a co-simulation platform was developed using MATLAB/Simulink and the Automated Driving Toolbox. Comparative experiments were conducted under representative conflict conditions reconstructed from NAIS accident data. The evaluation focuses on whether the algorithm can generate interpretable risk perception and controllable collision-avoidance trajectories under reproduced crash initial conditions, while also exhibiting behavioral differences under different driving-style parameterizations. To ensure physical fidelity, the geometric dimensions and dynamic constraints of all traffic participants were calibrated strictly according to the real vehicle data reported in NAIS.

5.1. Simulation analysis

Case 1: As shown in Fig. 8a, the human driver in the original Audi crash failed to perceive the laterally approaching vehicle and maintained a speed of 23 km/h, causing the risk to keep increasing and eventually leading to a collision. In contrast, the proposed method triggers braking as soon as the perceived risk is about to exceed the safety threshold, quickly reducing the ego speed from 23 km/h to approximately 4 km/h. This fast closed-loop "perception–braking" response pushes the risk back into the safe region before the physical conflict occurs, demonstrating the predictability of the proposed approach.

Figure 8b presents the final collision-avoidance trajectory. Benefiting from the proactive deceleration, the ego vehicle successfully yields to the obstacle vehicle rushing into the intersection. Trajectory analysis shows that the minimum center-to-center distance between the two vehicles during interaction is 4.46 m. Considering the vehicle dimensions, this indicates that sufficient physical clearance is maintained throughout the maneuver, confirming collision-free and safe passage even under extreme conditions.

Case 2: As shown in Fig. 9a, the VW driver in the original crash hesitated despite the low-risk oncoming through vehicle and was rear-ended by the following BMW driver who attempted to maintain safe headway. Under the proposed algorithm, although the perceived risk increases as the oncoming vehicle approaches, it remains below the risk threshold. The system therefore judges the situation to be within an acceptable risk range and suppresses overly conservative deceleration. After a brief adjustment, the ego speed recovers smoothly, avoiding the sustained slowdown and traffic obstruction caused by hesitation in the original crash.

The improved stability of ego decision-making also enhances the safety of the following vehicle. Figure 9b compares the follower's acceleration responses in two scenarios. In the original crash, the front vehicle hesitation forced the following vehicle into emergency braking (with a pronounced peak), triggering a rear-end collision. With the proposed method, the smoother trajectory requires only minor speed adjustments from the follower, substantially reducing the maximum deceleration demand and eliminating the rear-end risk, which validates the effectiveness of the method in improving interaction stability.

5.2. Validation of adaptive decision-making with different driving styles

To verify the effectiveness of the proposed RHT closed-loop mechanism under different driving-style settings, a typical Dynamic Left-Turn Game Scenario was constructed. The experiment aims to test whether the Comfort and Standard configurations produce the expected differentiated behaviors when facing the same critical gap (with specific parameter settings detailed in Table 3).

The scenario is configured as follows: the ego vehicle starts from rest; an oncoming through vehicle approaches the conflict point with a given distance and speed. This setting yields a critical time gap of about 4.5 s, lying near the decision boundary

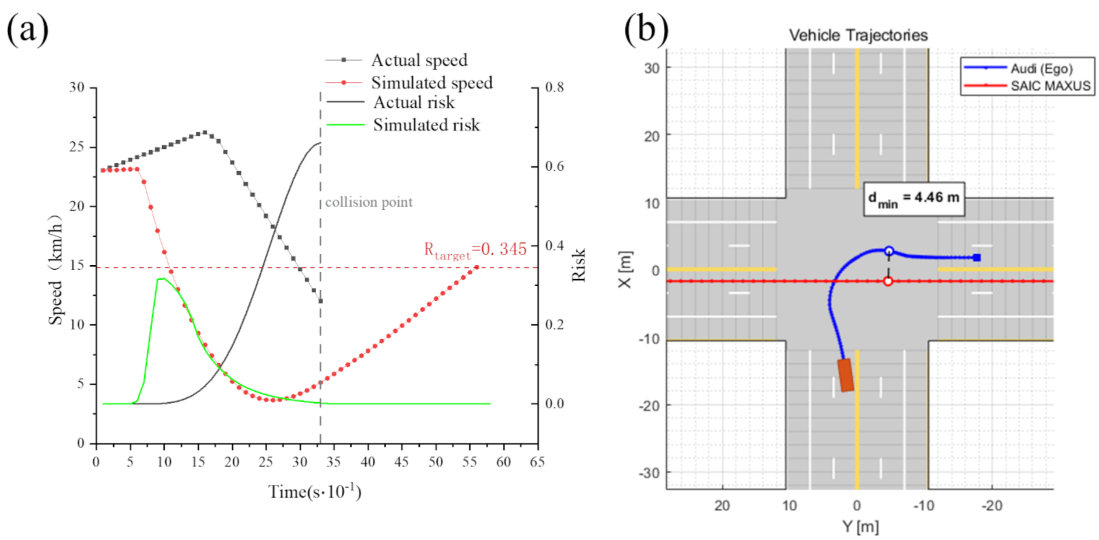

Fig. 8. Collision avoidance performance in Case 1: (a) Comparison of speed and risk profiles. The proposed method initiates early braking upon risk detection ($t \approx 0.8$ s), preventing the collision that occurred in the original case. (b) Vehicle trajectories. The ego vehicle yields to the obstacle, maintaining a safe clearance with $d_{\min} = 4.46$ m

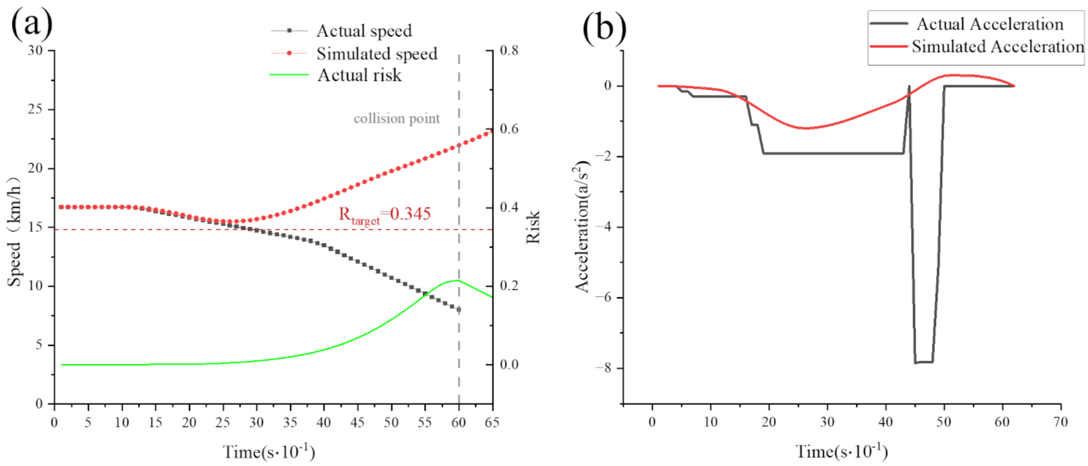

Fig. 9. Performance analysis in Case 2: (a) Decision-making process. The perceived risk remains below the target threshold ($R_{\text{target}} = 0.345$), allowing the ego vehicle to proceed smoothly without unnecessary hesitation. (b) Following vehicle response. The proposed method results in smooth deceleration, eliminating the emergency braking maneuver (-7.85 m/s^2) observed in the original crash case

Table 3
Parameter settings for different driving styles

Parameter	Symbol	Comfort style	Standard style
Target risk	R_{target}	0.300	0.400
Safety weight	w_{safety}	High	Normal
Smooth weight	w_{smooth}	High	Low
Efficiency weight	w_{eff}	Low	High
Speed limit gain	K_{pv}	0.6	1.2

Note: The linguistic descriptors ("High", "Normal", "Low") for the weights denote the relative priority magnitudes within the multi-objective cost function rather than absolute numerical values. This qualitative tuning logic is designed to penalize violations differently, thereby generating the distinct driving behaviors associated with the Comfort and Standard styles.

between "gap acceptance" and "yield," and thus clearly highlighting the decision differences induced by different risk thresholds.

Under the same simulation setting, the trajectory and dynamic responses of the two styles are compared in Fig. 10.

The results indicate that, for the same critical conflict conditions, different target risk thresholds lead to markedly different trade-offs between traffic efficiency and subjective safety.

Standard: As indicated by the blue trajectory in Fig. 10a, with a higher target risk and a larger efficiency weight, the planner tends to proceed when the rising risk remains below the configured threshold. The vehicle completes the left turn in 5.5 s (at a relatively higher average speed), reflecting an efficient and decisive gap-acceptance behavior typical of experienced drivers under high-throughput demand.

Comfort: The comfort setting strictly adheres to the lower target risk threshold (0.300). When the oncoming vehicle closes in, the RHT feedback triggers a rolling-yield decision. As shown in Fig. 10b, instead of hard braking, the ego vehicle smoothly reduces speed from 10 km/h to around 5.5 km/h to wait and then accelerates after the oncoming vehicle clears the conflict zone, and the risk naturally drops. Although the total passing time increases to 9 s, the maneuver avoids aggressive accel-

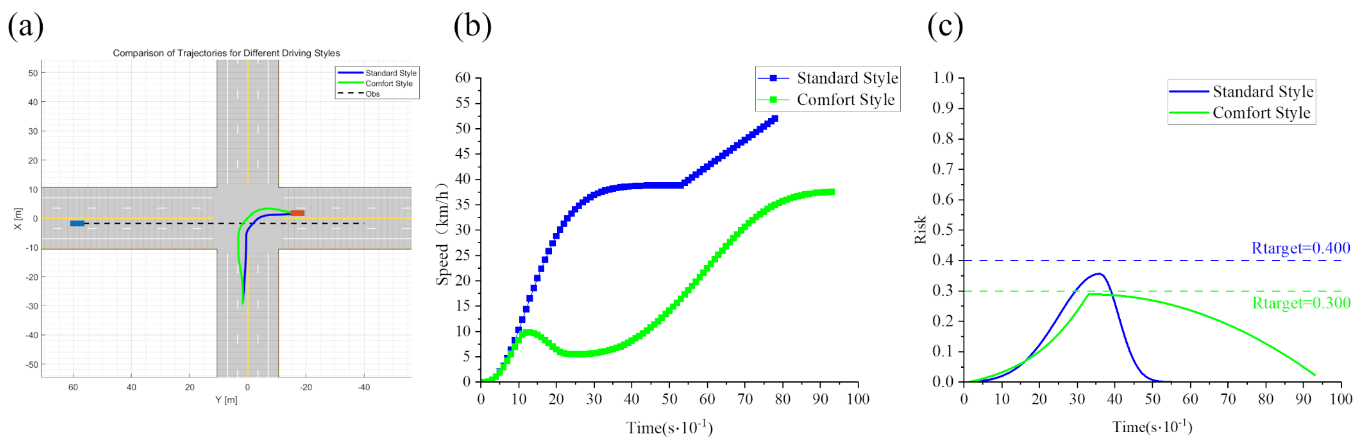

Fig. 10. Verification of driving style comparison: (a) trajectory comparison; (b) speed comparison; (c) risk comparison

eration/deceleration bargaining and prioritizes safety and ride comfort.

6. CONCLUSION AND FUTURE WORK

To address the long-standing difficulty of balancing efficiency and safety in permissive-phase left turns, this paper proposes an adaptive trajectory planning method grounded in Risk Homeostasis Theory (RHT). By fusing an RFS-based dynamic occupancy grid with a Driving Risk Field (DRF), the method provides a continuous quantification of both perception uncertainty and latent interaction risk. On top of this representation, a closed-loop perception–evaluation–planning feedback mechanism is constructed to monitor risk error in real time and adaptively regulate the planning-layer speed limit and safety buffer distance, thereby alleviating the decision rigidity caused by fixed parameters in conventional planners.

Reconstruction and simulation experiments based on real NAIS crash data show that the proposed approach delivers strong collision-avoidance capability under extreme conflict conditions, compensating for typical human limitations in complex interaction games and preventing both side-impact crashes induced by aggressive gap forcing and rear-end crashes caused by hesitation. The results further indicate that, by configuring different target risk thresholds and cost weights, the system can reproduce two representative human-like driving styles: decisive gap acceptance under a higher risk threshold, and smooth rolling yield under a lower threshold. This demonstrates a quantifiable balance between objective physical safety and subjective ride comfort, offering a practical way to manage the safety–efficiency trade-off in autonomous driving decision-making.

Despite these results, the study is still constrained by the current experimental setting. Future work will (i) further validate robustness in more complex urban conditions, such as multi-obstacle mixed traffic, pedestrian–vehicle mixing, and unsignalized roundabouts; (ii) explore an online style-identification mechanism based on inverse reinforcement learning (IRL), so that the target risk threshold can be adapted using passenger feedback or historical data toward truly personalized driving; and (iii) to strengthen the calibration of the Target Risk Threshold for real-world deployment, this algorithm will be integrated into standardized ADAS system testing pipelines. By building structured test scenarios on proving grounds and generating empirical data for ADAS performance evaluation, the baseline risk thresholds can be rigorously calibrated under controlled physical environments prior to mass deployment. This step will explicitly account for nonlinear dynamics (e.g., road friction) that affect plan execution, thereby bridging the gap between simulation and engineering applicability.

REFERENCES

[1] N. Stamatiadis, K.R. Agent, and A. Bizakis, "Guidelines for left-turn phasing treatment," *Transp. Res. Rec.*, vol. 1605, no. 1, pp. 1–7, 1997, doi: 10.3141/1605-01.

[2] J.M. Hutton, K.M. Bauer, C.A. Fees, and A. Smiley, "Evaluation of left-turn lane offset using the naturalistic driving study data," *J. Saf. Res.*, vol. 54, pp. 5.e1–15, 2015, doi: 10.1016/j.jsr.2015.06.016.

[3] X. Wang and M. Abdel-Aty, "Modeling left-turn crash occurrence at signalized intersections by conflicting patterns," *Accid. Anal. Prev.*, vol. 40, no. 1, pp. 76–88, 2008, doi: 10.1016/j.aap.2007.04.006.

[4] Y. Mao *et al.*, "A measurement to driving situation awareness in signalized intersections," *Transp. Res. Part D: Transp. Environ.*, vol. 62, pp. 739–747, 2018, doi: 10.1016/j.trd.2018.05.001.

[5] M. Abdel-Aty *et al.*, "Identification of intersections' crash profiles/patterns," *Florida Dept. Transp.*, Tallahassee, USA, Final Rep. BD544-12, 2006.

[6] Y. Matsui and S. Oikawa, "Characteristics of dangerous scenarios between vehicles turning right and pedestrians under left-hand traffic," *Appl. Sci.*, vol. 13, no. 7, p. 4189, 2023, doi: 10.3390/app13074189.

[7] L. Westhofen *et al.*, "Criticality metrics for automated driving: A review and suitability analysis of the state of the art," *Arch. Comput. Methods Eng.*, vol. 30, no. 1, pp. 1–35, 2023, doi: 10.1007/s11831-022-09788-7.

[8] S. Lefèvre, D. Vasquez, and C. Laugier, "A survey on motion prediction and risk assessment for intelligent vehicles," *ROBOMECH J.*, vol. 1, no. 1, pp. 1–14, 2014, doi: 10.1186/s40648-014-0001-z.

[9] M. Buehler, K. Iagnemma, and S. Singh, Eds., *The DARPA urban challenge: Autonomous vehicles in city traffic*, vol. 56. Berlin, Germany: Springer, 2009.

[10] D. Nuss *et al.*, "A random finite set approach for dynamic occupancy grid maps with real-time application," *Int. J. Robot. Res.*, vol. 37, no. 8, pp. 841–866, 2018.

[11] H. Jang, T. Kim, K. Ahn, S. Jeon, and Y. Kang, "Dynamic occupancy grid map with semantic information using deep learning-based BEVFusion method with camera and LiDAR Fusion," *Sensors*, vol. 24, no. 9, p. 2828, 2024, doi: 10.3390/s24092828.

[12] J. Wang, J. Wu, and Y. Li, "*The driving safety field based on driver–vehicle–road interactions*," *IEEE Trans. Intell. Transp. Syst.*, vol. 16, no. 4, pp. 2203–2214, 2015.

[13] T. Mullakkal-Babu, M. Wang, B. Van Arem, and R. Happee, "Probabilistic field approach for highway driving risk assessment," *IEEE Trans. Intell. Transp. Syst.*, vol. 21, no. 11, pp. 4611–4623, 2020.

[14] Y. Wang, Z. Sun, and D. Cao, "A probabilistic driving risk field for motion planning in unstructured environments," *IEEE Trans. Intell. Veh.*, vol. 8, no. 1, pp. 627–638, 2023.

[15] M. Werling, J. Ziegler, S. Kammel, and S. Thrun, "Optimal trajectory generation for dynamic street scenarios in a Frenet Frame," in *Proc. IEEE Int. Conf. Robot. Autom.* (ICRA), 2010, pp. 987–993.

[16] X. Li, Z. Sun, D. Cao, Z. He, and Q. Zhu, "Real-time trajectory planning for autonomous urban driving: Framework, algorithms, and verifications," *IEEE/ASME Trans. Mechatron.*, vol. 21, no. 2, pp. 740–753, 2016.

[17] P. Falcone, F. Borrelli, J. Asgari, H.E. Tseng, and D. Hrovat, "Predictive active steering control for autonomous vehicle path following," *IEEE Trans. Control Syst. Technol.*, vol. 15, no. 3, pp. 566–580, 2007, doi: 10.1109/TCST.2007.894643.

[18] J. Ziegler *et al.*, "Making Bertha Drive – An autonomous journey on a historic route," *IEEE Intell. Transp. Syst. Mag.*, vol. 6, no. 2, pp. 8–20, 2014, doi: 10.1109/MITS.2014.2306552.

[19] L. Chen, P. Wu, K. Chitta, B. Jaeger, A. Geiger, and H. Li, "End-to-end autonomous driving: Challenges and frontiers," *IEEE Trans. Pattern Anal. Mach. Intell.*, vol. 46, no. 12, pp. 10164–10183, Dec. 2024.

[20] S. Sharifzadeh, I. Chiotellis, R. Triebel, and D. Cremers, "Inverse reinforcement learning for autonomous driving," in *Proc. IEEE Intell. Veh. Symp.* (IV), 2016, pp. 1025–1030, doi: 10.1109/IVS.2016.7535514.

[21] L. Sun, W. Zhan, and M. Tomizuka, "Probabilistic prediction of interactive driving behavior via hierarchical inverse reinforcement learning," in *Proc. IEEE Int. Conf. Robot. Autom.* (ICRA), 2018, pp. 2111–2117, doi: 10.1109/ICRA.2018.8460544.

[22] G.J.S. Wilde, "The theory of risk homeostasis: Implications for safety and health," *Risk Anal.*, vol. 2, no. 4, pp. 209–225, 1982, doi: 10.1111/j.1539-6924.1982.tb01384.x.

[23] X. Wang, M. Wu, M. Abramson, and D.S. Hurwitz, "Crash reconstruction and analysis of left-turn conflicts at signalized intersections," *Accid. Anal. Prev.*, vol. 150, p. 105898, Feb. 2021, doi: 10.1016/j.aap.2020.105898.

[24] X. Wang, J. Yang, C. Zhang, and W. Wang, "A comprehensive study of intersection crash characteristics in Shanghai, China," *Traffic Inj. Prev.*, vol. 20, no. sup2, pp. 1–6, Oct. 2019, doi: 10.1080/15389588.2019.1661675.

[25] G. Lu, J. Hua, H. Zhao, M. Liu, J. Xu, and F. Zong, "Modeling vehicle paths at intersections: A unified approach based on entrance and exit lanes," *IEEE Trans. Intell. Transp. Syst.*, vol. 24, no. 12, pp. 14097–14110, Dec. 2023, doi: 10.1109/TITS.2023.3297151.

[26] H. Tan, G. Lu, and M. Liu, "Risk field model of driving and its application in modeling car-following behavior," *IEEE Trans. Intell. Transp. Syst.*, vol. 23, no. 8, pp. 11605–11620, Aug. 2022, doi: 10.1109/TITS.2021.3105432.

[27] J. Hua, G. Lu, and H.X. Liu, "Modeling and simulation of approaching behaviors to signalized intersections based on risk quantification," *Transp. Res. Part C: Emerg. Technol.*, vol. 142, p. 103773, 2022, doi: 10.1016/j.trc.2022.103773.